



The effect of post-irradiation annealing on the stress corrosion crack growth rate of neutron-irradiated 304L stainless steel in boiling water reactor environment

Wenjun Kuang^{a,b,*}, Justin Hesterberg^b, Gary S. Was^b

^a Center for Advancing Materials Performance from the Nanoscale (CAMP-Nano), State Key Laboratory for Mechanical Behavior of Materials, Xi'an Jiaotong University, Xi'an 710049, PR China

^b Department of Nuclear Engineering and Radiological Sciences, University of Michigan, Ann Arbor, MI 48109, United States

ARTICLE INFO

Keywords:

Stainless steel
SEM
Stress corrosion
Reactor conditions
Segregation

ABSTRACT

The effect of post-irradiation annealing (PIA) on the irradiation-assisted stress corrosion cracking (IASCC) of 304L stainless steel in boiling water reactor environments was studied. PIA has little effect on the crack growth rate (CGR) in normal water chemistry even it restored most of the irradiation-induced microstructure change. Nevertheless, PIA can significantly suppress the CGR in hydrogen water chemistry (HWC). The mitigation factor of HWC increases with the degree of PIA up to 5 h at 550 °C and correlates with the recovery of Si segregation at grain boundary. PIA is an effective strategy for decreasing IASCC susceptibility in reducing water environment.

1. Introduction

Irradiation-assisted stress corrosion cracking (IASCC) is a major degradation mode of in-core components in light water reactors (LWRs). Irradiation enhances the stress corrosion cracking (SCC) susceptibility by inducing water radiolysis and persistent microstructure changes in the component [1]. Hydrogen water chemistry (HWC) has been widely applied to diminish the concentration of oxidizing species from the water radiolysis in boiling water reactors (BWR) by promoting the recombination of those oxidizing species with hydrogen, thus decreasing the corrosion potential below -230 mV (vs. standard hydrogen electrode (SHE)) [2,3]. However, optimizing water chemistry cannot eliminate IASCC and some crack growth rate (CGR) results show that HWC loses its mitigation effect when the irradiation-induced damage exceeds a certain level [4]. The limited mitigation capacity of water chemistry on IASCC is evident in the elevated CGR in irradiated stainless steel (SS) in low potential, pressurized water reactor (PWR) primary water [5].

Post-irradiation annealing (PIA) is a strategy to mitigate IASCC as it can progressively remove the irradiation-induced damage (dislocation loops, radiation-induced segregation (RIS) and precipitates) with increasing annealing time and temperature [6–11]. Moreover, it may provide an opportunity to single out the dominant microstructure feature controlling IASCC susceptibility since irradiation-induced defects

recover at different rates. The mitigation effect of PIA on IASCC has been evaluated most using constant extension rate tensile (CERT) or constant deflection tests. Jacobs et al. [12] found that the IGSCC percentage of 304 SS in CERT tests (irradiated to $2.75\text{--}2.9 \times 10^{21}$ n/cm², $E > 1$ MeV) in a simulated BWR environment decreased with annealing temperature (from 400 to 500 °C) and with time at 500 °C. In their study, the intergranular stress corrosion cracking (IGSCC) resistance was fully restored after 1 h at 500 °C while the ductility was only partially restored [12]. Katsura et al. [6] reported that the IGSCC percentage of 304 SS (irradiated to 1.2×10^{22} n/cm², $E > 1$ MeV) in a BWR environment decreased from 95% to 45% as the annealing temperature was increased from 400 to 500 °C while that of a 316 SS (irradiated to 8×10^{25} n/cm², $E > 1$ MeV) dropped to 0% after 1 h at 450 °C. CERT tests conducted by Fukuya et al. [7] also showed that the IASCC susceptibility of cold-worked 316 SS irradiated to 25 dpa in a simulated PWR primary water decreased with increasing annealing temperature. The CERT and four-point bend tests on the same batch of samples as used in this work revealed that PIA at 500 or 550 °C progressively reduced IASCC susceptibility in NWC environment [13].

While CERT test results have clearly demonstrated the beneficial effects of PIA in mitigating IASCC initiation, CGR tests are still needed to evaluate the effects of PIA on the SCC propagation of irradiated materials in different environments and thus the HWC mitigation factor. From the CGR disposition curves for as-irradiated SS (0.57–4.5

* Corresponding author at: Center for Advancing Materials Performance from the Nanoscale (CAMP-Nano), State Key Laboratory for Mechanical Behavior of Materials, Xi'an Jiaotong University, Xi'an 710049, PR China.

E-mail address: wjkuang66@gmail.com (W. Kuang).

<https://doi.org/10.1016/j.corsci.2019.108183>

Received 12 May 2019; Received in revised form 30 July 2019; Accepted 25 August 2019

Available online 26 August 2019

0010-938X/ © 2019 Elsevier Ltd. All rights reserved.

dpa) [14], the CGRs in both NWC and HWC have the same K dependence and the HWC mitigation factor (CGR_{NWC}/CGR_{HWC}) is 3, which is smaller than that from non-irradiated materials [3]. A previous work indicates that the HWC mitigation effect on the CGR of irradiated SS vanished when the dose was above ~ 6 -7 dpa [4]. However, Chimi [15] reported that adding ~ 2 ppm H_2 could mitigate the CGR of 304 L SS irradiated to 7.7 dpa by a factor over 10 in 325 °C water and PIA at 500 or 550 °C for 25 h could further enhance the mitigation factor in 280 °C water although it had little effect on the CGR in oxygenated water. It is difficult to establish whether PIA could affect CGRs in different environments and restore the mitigating effect of HWC on highly irradiated material from such limited data. More importantly, the microstructure features responsible for the environment dependence of PIA effect on CGR has not been determined yet. Some research efforts have been made to isolate the effects of segregated impurity elements on CGR using model alloys doped with different levels of impurities. The results indicate that Si has a major role in promoting CGR. Li et al. [16] found that Si could significantly accelerate the intergranular CGR of austenitic steels in 325 °C primary water. Consistently, Andresen and Morra [17] reported that Si dramatically increased the CGR of 304 L SS in HWC and reduced the effects of stress intensity factor. Nevertheless, the direct correlation between the CGR data and microstructure features from irradiated sample are much needed.

This work is intended to study the effects of PIA on CGR of neutron-irradiated 304 L SS in a BWR environment. The efficacy of HWC will be evaluated for different annealing conditions and the mitigation effect will be discussed in relation to the microstructure changes.

2. Experimental

2.1. Material

Neutron-irradiated samples of 304 L SS were machined from a control rod (#1690) used in the Barsebäck 1 BWR in Sweden for the entirety of its operational lifetime. The control rod was manufactured from solution-annealed 304 L SS. The chemical composition of the un-irradiated material in both weight percentage and atomic percentage is shown in Table 1 [4]. The mechanical properties of the non-irradiated alloy have been determined previously via tensile experiments at both room temperature and 300 °C [4]. The average yield stress at 300 °C is around 169 MPa with a total elongation of 42%.

The damage accumulated in the region of the control rod from which samples were taken was 5.9 dpa. The temperature during irradiation was estimated to be 288 °C. Tensile tests have been performed in air at 288 °C on samples machined from this control rod and the average yield stress is around 672 MPa with a total elongation of 11.2% [4].

2.2. Sample machining and PIA treatment

Four round compact tensile (RCT) samples were machined from the control rod. The schematic of the RCT is shown in Fig. 1 and the dimensions are listed in Table 2. The samples were machined with 5% side grooves on each side. The PIA conditions along with the sample IDs are also listed in Table 2. Three PIA treatments were applied: 1 h at 500 °C, 5 h at 550 °C and 20 h at 550 °C. The annealing treatments were conducted in a standard air furnace, which demonstrated a good temperature stability. The specimens were all removed from the furnace

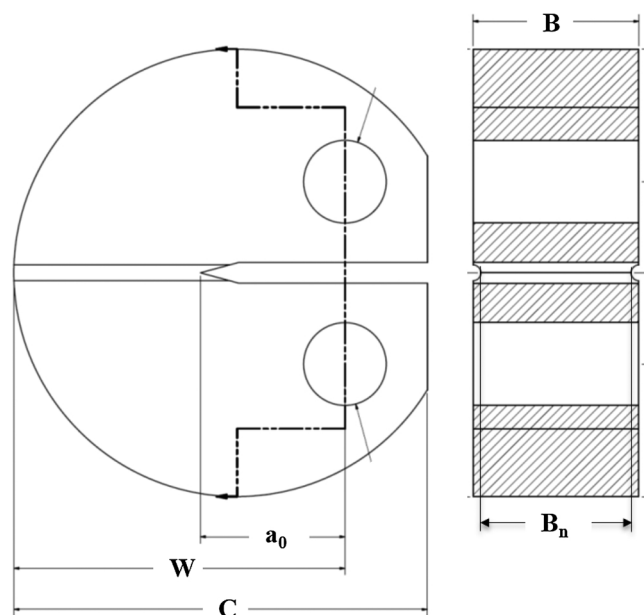


Fig. 1. Schematic showing the geometry and dimensions of the RCT sample.

Table 2

Annealing conditions, yield stresses (YS) (in MPa) [4] and dimensions (in mm) of the RCT samples.

Sample ID	Annealing condition	YS at 288 °C	W	C	a_0	B	B_n
R1	As-irradiated	685.5	16.14	20.03	6.43	8.05	7.36
R2	500 °C, 1 h	633.4	16.30	19.89	6.83	8.08	7.19
R3	550 °C, 5 h	483.6	16.03	20.02	6.33	8.05	7.31
R4	550 °C, 20 h	421.3	16.10	19.99	6.52	8.06	7.30

within 2 min of their targeted annealing times.

2.3. CGR test system

The CGR tests were conducted in Irradiated Materials Testing Complex (IMTC) at the University of Michigan which consists of the Irradiated Materials Testing Laboratory and two fully equipped hot cells. The test system consists of a refreshed water loop and a 4-liter 316 SS autoclave. The CGR tests were conducted in simulated BWR environments, including both normal water chemistry (NWC) and HWC. Temperature and pressure of the simulated environments were 288 °C and 10.3 MPa, respectively. The water in the autoclave was refreshed three times per hour with a flow rate of 180 mL/min. Dissolved oxygen (DO) and conductivity of inlet/outlet water were continuously monitored using a Thornton 770Max DO/conductivity meter. The outlet conductivity was controlled to 0.1 μ S/cm by adding diluted sulfuric acid into the water reservoir. Inlet DO was controlled at 2 ppm for NWC and dissolved hydrogen (DH) was controlled at about 100 ppb for HWC.

The direct current potential drop (DCPD) technique was used to monitor the change in crack length. As the samples were radioactive, they were loaded in hot cell #1 and current and potential leads (Pt wires) were spot-welded onto the RCT sample with a specially designed fixture by manipulator arms. Zirconia sleeves were used to electrically

Table 1

Chemical composition of the 304 SS control rod in un-irradiated condition based on ladle analysis [4].

Element	C	Si	Mn	Cr	Co	N	Ni	P	S	Fe
Wt.%	0.025	0.30	1.09	18.35	0.029	0.024	10.57	0.013	0.003	Bal.
At.%	0.11	0.59	1.09	19.45	0.03	0.09	9.92	0.02	0.005	Bal.

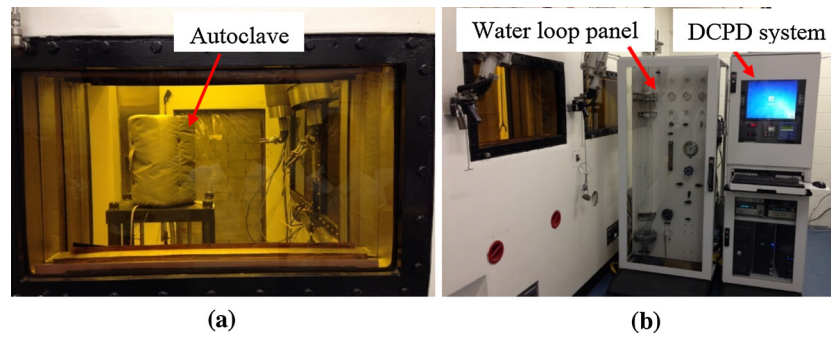


Fig. 2. Images of the crack growth rate test system.

isolate the sample from the loading pins and the autoclave containing the RCT sample was closed and moved to hot cell #2 for testing. The water loops and controls remained outside of the hot cell for easy access during the experiment. Fig. 2 shows images of the test system in hot cell #2.

The DCPD monitoring system consists of a DC power supply, relays, nano-volt meter, data acquisition unit, and a servomotor. DC power supply provided a stable current (2.5 A) to the specimen. The current was reversed once per second through solid-state relays to correct for thermocouple effects. The potential drop resulting from crack propagation in the specimen was measured by a nano-volt meter. The electrochemical potential (ECP) of the RCT specimen was continuously monitored during the CGR test with a Cu/Cu₂O reference electrode. At the same time, the redox potential between a 1.0 cm² Pt flag and the reference electrode was also recorded.

2.4. CGR test procedure

The CGR test was conducted to determine both the K dependence and the effect of environment change on CGR. To compare the SCC susceptibility between different samples, tests were conducted at the same K levels. According to ASTM E399, the applied K values should meet the validity criterion to ensure mainly plane strain conditions at the crack tip:

$$(K/\sigma_{YS})^2 < W-a \text{ and } B_{\text{eff}} \quad (1)$$

where σ_{YS} is the yield strength of the 304 L SS, $W-a$ is the remaining length of the crack and B_{eff} is the effective thickness of the sample. For irradiated samples, the effective σ_{YS} is normally taken as:

$$\sigma_{YS} = \sigma_{YS(\text{unirrad})} + (\sigma_{YS(\text{irrad})} - \sigma_{YS(\text{unirrad})})/2 \quad (2)$$

or

$$\sigma_{YS} = \sigma_{YS(\text{unirrad})} + (\sigma_{YS(\text{irrad})} - \sigma_{YS(\text{unirrad})})/3 \quad (3)$$

where $\sigma_{YS(\text{irrad})}$ is the yield strength of the irradiated material and $\sigma_{YS(\text{unirrad})}$ is the yield strength of its unirradiated counterpart. Currently, there is not an agreed-upon method of calculating the effective yield strength of irradiated materials, though Eq. (3) is generally preferred for highly irradiated material with little work hardening capacity. As the annealed samples possess different work hardening behaviors, different ways for calculating the effective yield strength were used. For the samples with limited work hardening such as R1 (as-irradiated) and R2 (500 °C, 1 h), Eq. (3) was used. For R3 (550 °C, 5 h) with greater work hardening capacity, Eq. (2) was used. The yield strength of R4 (550 °C, 20 h) was used directly in Eq. (1) as this post-irradiation heat treatment removed much of the irradiation-induced strengthening.

Based on the K validity check for the expected behavior of the as-irradiated sample and R4, three nominal K values were selected for CGR testing: 18, 14 and 11 MPa·m^{1/2}. The test steps for each sample are listed in Table 3. The sample was pre-cracked from the machined notch

Table 3
Planned test steps for CGR tests.

Step	Water chemistry	Stress intensity (MPa·m ^{1/2})	Waveform	Intended crack growth (mm)
1	BWR NWC	18	Haversine ($R = 0.4$, $f = 0.5$ Hz)	~0.4
2	BWR NWC	18	Haversine ($R = 0.6$, $f = 0.1$ Hz)	0.1
3	BWR NWC	18	Haversine ($R = 0.6$, $f = 0.01$ Hz)	0.1
4	BWR NWC	18	Haversine ($R = 0.6$, $f = 0.001$ Hz)	0.1
5	BWR NWC	18	Trapezoid	0.1
6	BWR NWC	18	Constant K	0.09
7	BWR HWC	18	Constant K	0.09
8	BWR NWC	18	Constant K	0.09
9	BWR NWC	18 to 14	Trapezoid	0.128
10	BWR NWC	14	Constant K	0.09
11	BWR NWC	14 to 11	Trapezoid	0.128
12	BWR NWC	11	Constant K	0.09
13	BWR HWC	11	Constant K	0.09

by fatigue, as shown in Table 3, where a low load ratio, $R = 0.4$, and high frequency, $f = 0.5$ Hz, were used to introduce cracking at a fast rate. The maximum K was slightly lower than or equal to that used for the first constant K step. Later, to initiate the transition from transgranular to intergranular fracture, R was increased to 0.6 and f was incrementally lowered to 0.01 and then 0.001 Hz. After the fatigue step at 0.001 Hz, a trapezoidal load form was applied with a hold time of 9000 s. Subsequently, the test was run under constant K control.

To maintain a constant K value during the test, the applied load was automatically adjusted once a minimum increment of 0.001 in a/W was achieved. The environment was switched from NWC to HWC when the CGR stabilized and the crack increment at constant K exceeded 0.09 mm, which is considered statistically meaningful [3]. Although a growth of ~0.09 mm is also desirable in HWC, this is unrealistic due to the very low CGR. Therefore, the test was run in HWC until a stable CGR was acquired, after which, the environment was switched back to NWC.

When changing the K value, it was very important to sustain the crack growth during the transition period. dK/da control was used to ensure a smooth transition for decreasing K , for which a trapezoid waveform was normally used. The rate of change of K with a (dK/da) is calculated based on the a/W and K values from two neighboring steps. Thus, the dK/da values are a little different between K changes from 18 to 14 MPa·m^{1/2} and 14 to 11 MPa·m^{1/2} (Table 3). As the crack grows, a change in K will be made based on the dK/da value. The threshold for the K change was set to 0.022 MPa·m^{1/2}.

Upon completion of the test, the autoclave system was cooled to room temperature. The sample was fully fractured by fatigue at room temperature. To minimize plastic deformation at the crack front, the K was controlled at the same or lower value compared to that last used in

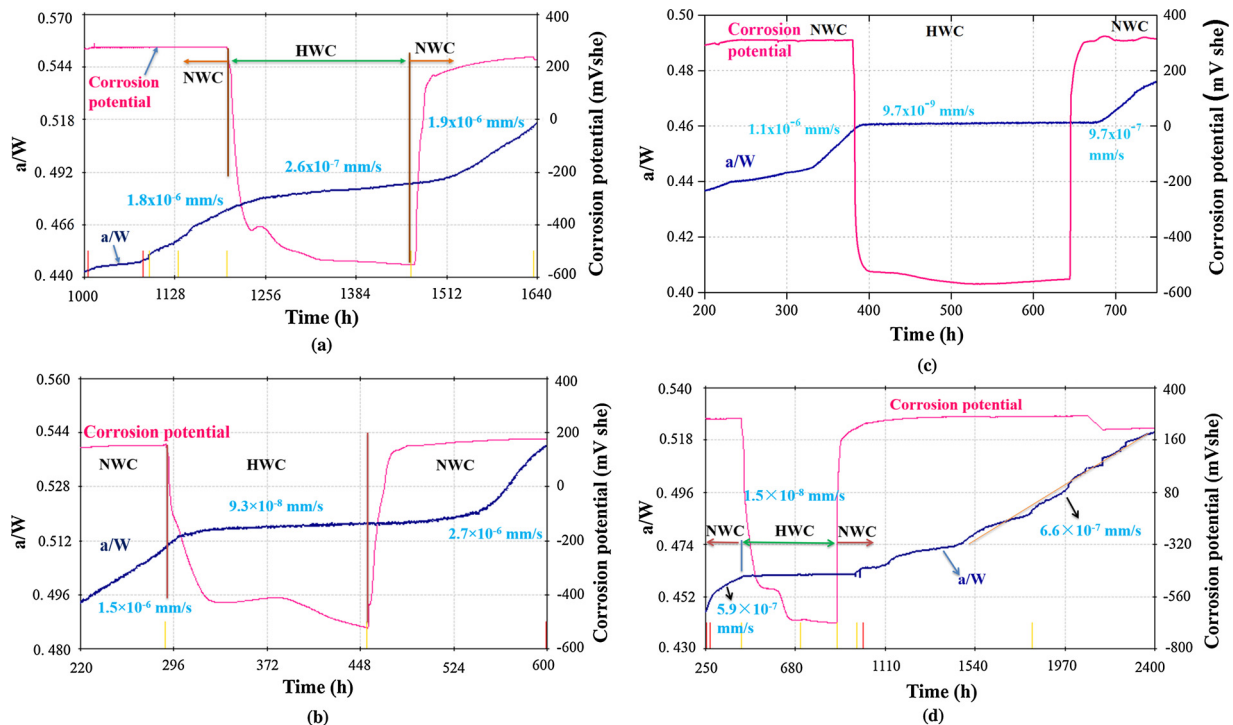


Fig. 3. Ratio of crack length over sample width (a/W) and corrosion potential of (a) R1, (b) R2, (c) R3 and (d) R4 in 288 °C water containing 2 ppm O_2 at a nominal K of $18 \text{ MPa}\cdot\text{m}^{1/2}$ during the change of corrosion potential.

high temperature water. After growing a post-test crack about 0.5 mm, the RCT specimen was fatigued at high frequency until fracture. The fracture surfaces of the RCT specimen were analyzed using a JOEL JSM-6480 scanning electron microscope (SEM). The areas of transgranular fracture during pre-cracking, and IGSCC fracture surface were measured and divided by the thickness of sample to calculate the average crack length for each area. The measured crack length from the fracture surface analysis was compared with that from the DCPD measurement. The ratio between the two measurements was used as correction factor for the crack length and crack growth rate. K was recalculated using the corrected crack length and the applied load, which was recorded in the data file.

3. Results

Fig. 3 shows the change in a/W (ratio of crack length to sample width) and corrosion potential at a nominal K of $18 \text{ MPa}\cdot\text{m}^{1/2}$ during the change from NWC to HWC and then back to NWC, or steps 6–8 in Table 3. The CGRs shown in these figures are post corrected. In NWC, the corrosion potential normally ranged between 160 and 300 mV (vs SHE). After the switch to HWC, the corrosion potential rapidly dropped to $-400 \sim -680$ mV. These potential ranges are consistent with those reported in previous works [3,18]. After switching back to NWC, the corrosion potential increased back to the original value, indicating a good control of the environment condition.

For R1 (Fig. 3a), the CGR stabilized at 1.8×10^{-6} mm/s in NWC and dropped to 2.6×10^{-7} mm/s after the switch. As the environment was switched back to NWC, the CGR increased to a value of 1.9×10^{-6} mm/s, which was very close to the previous value obtained in NWC. It should be noted that there was a time delay of about 40 h in the response of the CGR to the switch to NWC. For R2 (Fig. 3b), the CGR stabilized at 1.5×10^{-6} mm/s in NWC, then decreased to 9.3×10^{-8} mm/s after the switch to HWC. Upon switching back to NWC, the CGR increased up to 2.7×10^{-6} mm/s after a lag time of ~75 h. As for R3 (Fig. 3c), the CGR stabilized at 1.1×10^{-6} mm/s in NWC, then decreased to 9.7×10^{-9} mm/s upon switching to HWC. Thereafter, the

environment was switched back to NWC and the CGR increased back to 9.7×10^{-7} mm/s after a time lag of about 40 h. Again, the CGRs in NWC were very close to each other. The CGR of R4 stabilized at 5.9×10^{-7} mm/s in NWC (Fig. 3d), dropped to 1.5×10^{-8} mm/s after the switch to HWC and then stabilized at a value of 6.6×10^{-7} mm/s after a delay of ~650 h. The final CGR was very close to the previous value in NWC. There are some jumps in a/W (up to 0.002) which are due to the breakage of ligaments along the crack propagation path. Such jumps have also been reported in the results from the sample of the same heat [4]. Due to the presence of jumps in a/W , it took longer (~1350 h) to acquire a reliable average CGR. The ligaments will be discussed along with the fracture surface analysis.

The fracture surfaces of the four samples are shown in Fig. 4 and the measured crack lengths are summarized in Table 4. The fracture surface is intergranular except for the pre-cracked and post-cracked regions. For R1 (Fig. 4a), the front of pre-cracked region was uneven probably due to the inhomogeneity in microstructure, but the IGSCC region was mainly intergranular although there were some ligaments in the final stage (as shown in the insert). In R2, the pre-cracked region was fully transgranular and showed an even crack front (Fig. 4b). While the IGSCC region is primarily intergranular, the crack front of the IGSCC region contains a transgranular ligament near the middle, as shown in the insert. R3 also showed an even pre-crack front (Fig. 4c). The IGSCC region was fully intergranular although the crack front was crooked. No significant ligament was observed in the IGSCC region. For R4 (Fig. 4d), the large crack on the left side was due to post-test overloading. It should be noted that there was a large ligament between the upper part and the lower part in the IGSCC region which is represented by a black line on Fig. 4d. The enlarged image shows that the two parts of the IGSCC region are not on the same plane and the interface between them is a transgranular ligament that is almost perpendicular to the fracture surface. Such a ligament would not crack open until the opening of the main crack was larger than the distance between the two crack planes. The ligament would be a conductive path for DCPD current which could explain why DCPD underestimated the crack length on this sample (Table 4). The jumps in a/W (Fig. 3d) were likely due to sudden tearing

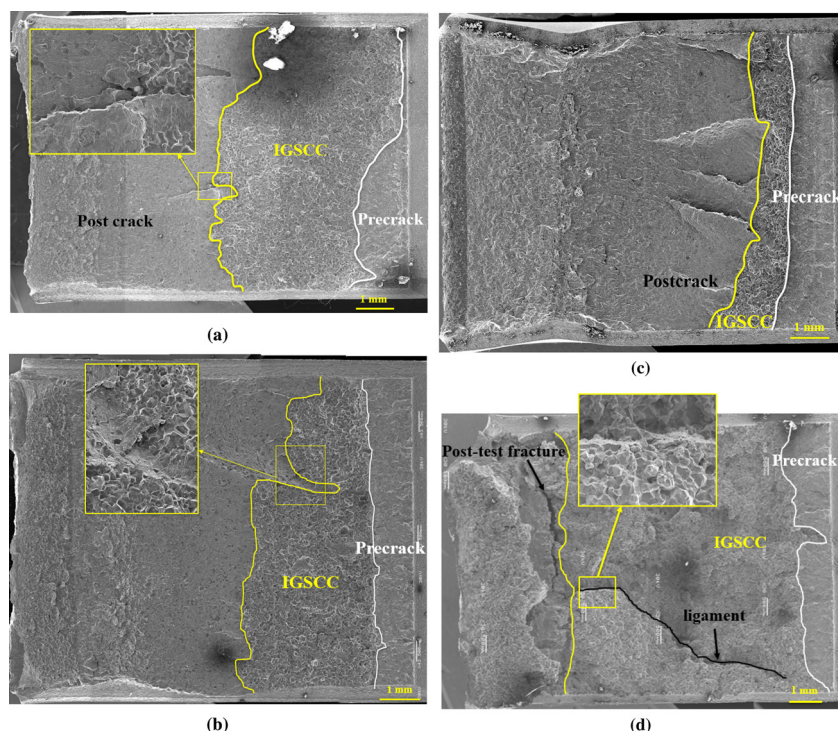


Fig. 4. Fracture surfaces of (a) R1, (b) R2, (c) R3 and (d) R4 after crack growth rate tests.

Table 4
Results of crack length measurements and correction factors after CGR tests.

	Pre-crack			IGSCC Crack		
	Length by DCPD (mm)	Length by SEM (mm)	Correction factor	Length by DCPD (mm)	Length by SEM (mm)	Correction factor
R1	0.775	0.737	0.95	2.073	3.83	1.85
R2	0.831	1.012	1.22	1.831	2.639	1.44
R3	0.802	1.103	1.38	1.234	1.076	0.87
R4	0.725	0.856	1.18	2.157	6.018	2.79

of the ligament. Higher mag SEM images on the fracture surfaces of R1, R2 and R3 were shown in Fig. 5. In addition to oxide particles on the faceted grain surfaces, extensive secondary intergranular cracks, as indicated by the arrows, were observed on all the samples.

The crack lengths measured by DCPD and SEM along with the correction factors are listed in Table 4. For the pre-crack, DCPD predicted the length fairly accurately. However, it tended to underestimate the IGSCC crack length, especially when there were ligaments on the crack path, as in the case of R4. This is a common issue when testing neutron-irradiated sample and some non-irradiated materials like nickel-based weld metals for the bottom parts of nuclear reactors [19]. The correction factors in Table 4 were used to correct K and CGR values for each step. The results are listed in Table 5. The K values were post-corrected based on the measured crack length and the applied load. For some steps, there is a small variation in the corrected K as the applied K was not ideally constant. The ranges of those corrected K values are listed in Table 5. The K validity was checked by calculating the ratio of corrected K over the maximum allowable K . The work by Jenssen et al. [20] suggests that the K limit by ASTM E399 can be exceeded by at least 20% for materials with significant strain hardening behavior. Although the samples used in this work were irradiated to 5.9 dpa, PIA restored some of the strain hardening capacity. Further, no unusually large increase in CGR was observed during the test. As such, the CGR was deemed valid if the K did not exceed the maximum allowable value by

more than 20%. According to this rule, two data points from R1 were tentatively considered invalid.

All the CGR data was plotted in Fig. 6. The error bars on K indicate the uncertainties of the corrected K value. Some data points have very small uncertainties, and the error bars are inside the symbols. The data from the same bulk material tested by Jenssen [4] was also included in the plot for comparison. The invalid data points from R1 are framed in dashed squares. The CGRs of the as-irradiated sample (R1) in NWC are very consistent with those from Jenssen at similar K values. However, the CGR in HWC is much higher than that reported in Jenssen's work [4]. Pathania et al. [14] proposed CGR disposition curves for irradiated SS in NWC and HWC environments, and these curves are represented by dashed and dash-dotted lines, respectively, in Fig. 6. Although the disposition curves were intended for a fluence range of 5×10^{20} – 30×10^{21} n/cm² (0.57–4.5 dpa), the CGRs from R1 (as irradiated to 5.9 dpa) in both NWC and HWC follow the curves very well except that at the lowest K value they fall below the curves, probably due to the formation of ligaments at the final stage, as shown in Fig. 4a. From Fig. 6, it is evident that the CGRs in NWC do not vary with PIA condition and follow the NWC disposition curve very well. Thus, it seems that the PIA treatment has little effect on the susceptibility of IASCC propagation in NWC. However, the HWC environment shows a significant effect in mitigating CGR on all the samples, with the HWC mitigation factor dependent on the PIA condition, as listed in Table 6. All the CGRs in HWC for the PIA samples fall below the HWC disposition curve. The CGRs of R1 (as-irradiated) and R2 (annealed at 500 °C for 1 h) were decreased by factors of 4⁷ and 16 respectively while those of R3 (annealed at 550 °C for 5 h) and R4 (annealed at 550 °C for 20 h) were reduced by factors in the range of 55–100, and 39 respectively in HWC. The mitigation effect of HWC increases with the extent of PIA treatment first and decreases a little from 5 to 20 h at 550 °C.

4. Discussion

The CGR results show that the mitigation effect of PIA treatment on the crack propagation of neutron-irradiated 304L SS depends on the environment. The effects of PIA on the SCC propagation process in both

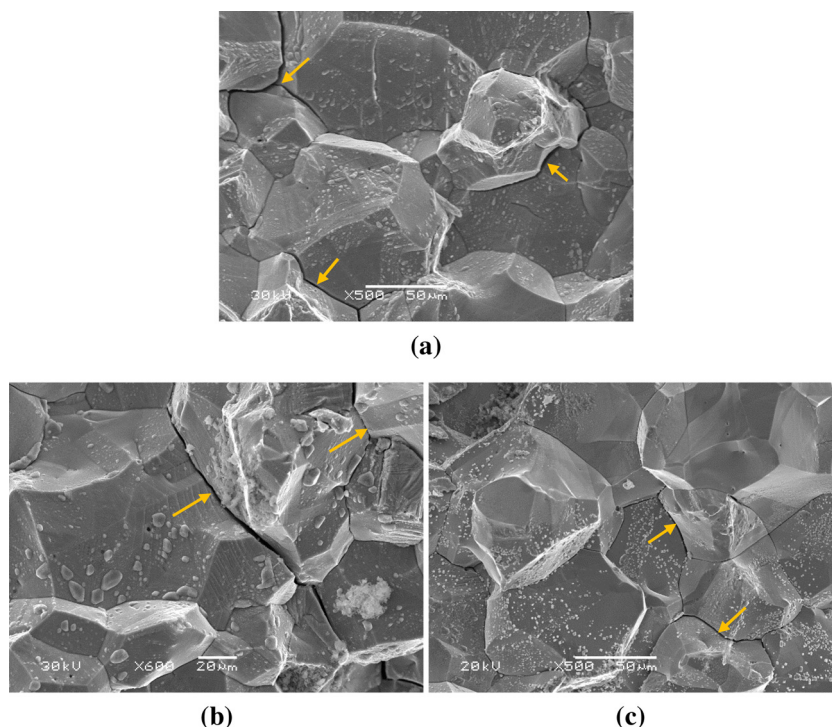


Fig. 5. SEM images of secondary cracks (indicated by arrows) from fracture surfaces of (a) R1, (b) R2 and (c) R3.

NWC and HWC environments will be discussed separately in relation to the microstructure changes. Then, the IASCC susceptibilities from CGR and CERT tests will be compared.

4.1. Environment dependence of PIA effect on CGR

CGR results from this work (Fig. 6) clearly show that the CGRs in NWC are very comparable at similar *K* values for as-irradiated and different PIA conditions, indicating that PIA does not have a significant

effect on the crack propagation susceptibility in NWC. Those data are also well described by the NWC disposition curve for SS irradiated to a similar dpa range. Interestingly, the dose dependence of CGR in NWC seems insignificant from the previous CGR data on neutron-irradiated 304 L SS over a dose range of 3 to 14 dpa [4]. The lack of a mitigation effect of PIA on CGR in NWC is interesting given the large changes in both yield strength and microstructure.

Table 2 shows that the yield stress decreases monotonically with the severity of PIA treatment. As for microstructure, a preceding study on

Table 5
Corrected *K* values and CGRs of RCT samples.

Sample	Environment	Δa^* (μm)	Corrected CGR (mm/s)	Corrected <i>K</i> ($\text{MPa}\cdot\text{m}^{1/2}$)	Max allowable <i>K</i> ($\text{MPa}\cdot\text{m}^{1/2}$)	Valid? **	<i>K</i> validity ratio ***, %		
							E399	$\Delta\text{YS}/2$	$\Delta\text{YS}/3$
R1	NWC	753	1.8×10^{-6}	17.9~19.1	18.9	Y			98
	HWC	179	2.6×10^{-7}	19.5~19.8	18.9	Y			104
	NWC	494	3.2×10^{-6}	23.3~25.0	16.9	N			143
	NWC	239	6.7×10^{-7}	20.1~20.9	16.0	N			128
	NWC	96	9.5×10^{-8}	17.0~17.3	15.5	Y			111
R2	HWC	18	2.3×10^{-8}	17.3~17.4	15.5	Y			112
	NWC	414	1.5×10^{-6}	119.55	17.8	Y			110
	HWC	52	9.3×10^{-8}	20.0	17.7	Y			113
	NWC	423	2.7×10^{-6}	20.6	17.3	Y			119
	NWC	235	8.2×10^{-7}	16.7	16.5	Y			101
R3	NWC	110	2.8×10^{-7}	13.9	15.7	Y			89
	HWC	16	1.8×10^{-8}	14.1	15.7	Y			90
	NWC	182	1.1×10^{-6}	19.2~19.3	18.1	Y		107	
	HWC	17	9.7×10^{-9}	19.3	18.1	Y		107	
	NWC	141	9.7×10^{-7}	19.4~19.5	18.1	Y		108	
R4	NWC	56	2.9×10^{-7}	14.6	18.1	Y		81	
	NWC	53	2.7×10^{-7}	11.4	18.1	Y		63	
	HWC	4	4.8×10^{-9}	11.4	18.1	Y		63	
	NWC	98	3.4×10^{-7}	11.3	17.9	Y		63	
	NWC	269	5.9×10^{-7}	18.9~19.5	23.3	Y	82		
R4	HWC	45	1.5×10^{-8}	19.5~19.6	23.3	Y	84		
	NWC	2784	6.6×10^{-7}	19.7~31.3	21.9	Y	117		

* The crack growth length for each stage was picked when the CGR stabilized.
 ** The CGR data is consider valid when the applied *K* value is less than 120% of the maximum allowable *K*.
 *** *K* validity ratio is the ratio of corrected *K* over the maximum allowable *K*.

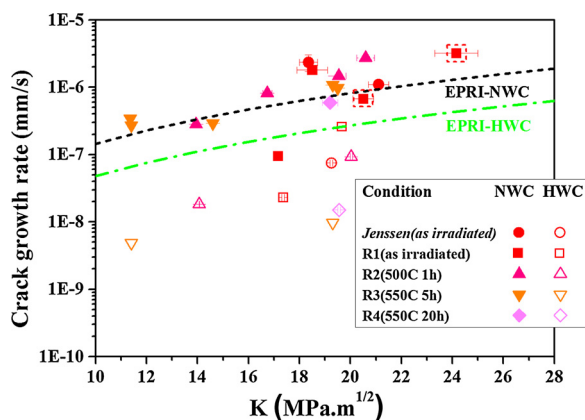


Fig. 6. Crack growth rates of 304L SS irradiated to 5.9 dpa in 288 °C water. Solid symbols refer to NWC and open symbols refer to HWC.

Table 6 Mitigation factors of HWC ((da/dt)_{NWC}/(da/dt)_{HWC}) on 304 L SS irradiated to 5.9 dpa in 288 °C water.

Sample	K (MPa·m ^{1/2})	NWC (mm/s)	HWC (mm/s)	Mitigation factor
From Jessen [4]	18.4~19.3	2.4E-06	7.5E-08	31.3
R1 (As-irradiated)	18.5~19.7	1.8E-06	2.6E-07	6.9
	17.2~17.4	9.5E-08	2.3E-08	4.1
R2 (500 °C, 1 h)	19.5~20.0	1.5E-06	9.3E-08	16.1
	13.9~14.1	2.8E-07	1.8E-08	15.6
R3 (550 °C, 5 h)	19.3	1.1E-06	9.7E-09	113.4
	11.4	2.7E-07	4.8E-09	56.2
R4 (550 °C, 20 h)	19.2~19.6	5.9E-07	1.5E-08	39.3

these same PIA conditions provided a detailed account of the irradiated microstructure [11]. The results summarized in Table 7 [11] indicated that the densities of dislocation loop and solute clusters decreased while the sizes of those features increased with the severity of PIA treatment. The average dislocation channel spacing generated after deformation decreased as well [13] with increasing extent of PIA. Significant recovery of RIS at grain boundaries was also observed after PIA at 550 °C [11], as shown in Table 8, although PIA at 550 °C for 20 h induced sensitization on some grain boundaries [13]. The recovery of mechanical properties and microstructure damages by PIA seems inconsistent with the CGR data in NWC based on the general understanding of SCC. It has been reported that the CGR of SS drops with decreasing yield strength [3,21]. The decrease in average dislocation channel spacing and recovery of Cr content at grain boundary should also improve the SCC resistance as the dislocation channel-grain boundary interaction is an important precursor for SCC initiation [22], and Cr depletion could aggravate SCC in simulated NWC environment [23,24]. Although the CGR in NWC was not affected by the PIA treatments, CGR in HWC tended to decrease with increasing degree of PIA (Fig. 6). The CGRs for the two samples annealed at 550 °C are almost the same although the 20 h annealing treatment induced sensitization on some grain boundaries [13], indicating that the mitigating effect saturated after a 5 h

Table 7 Summary of dislocation loop and solute clusters for different PIA conditions (d-average diameter, N-number density, L-line length density, f_v-volume fraction) [11].

	Dislocation Loop			Ni-Si Solute Cluster			Al-Cu Solute Cluster		
	d (nm)	N (10 ²² m ⁻³)	L (10 ¹⁵ m/m ⁻³)	d (nm)	N (10 ²³ m ⁻³)	f _v (%)	d (nm)	N (10 ²³ m ⁻³)	f _v (%)
As-Irradiated	8.3	11.1	2.89	9.2	3.9	2.5	5.7	2.9	0.035
500 °C, 1 h	9.6	8.2	2.47	10.8	2.8	2.4	6.2	2.5	0.027
550 °C, 5 h	8.0	1.3	0.32	18.1	1.2	3.6	11.0	2.6	0.041
550 °C, 20 h	26.0	0.05	0.04	20.2	0.7	3.0	13.2	0.9	0.016

Table 8 Grain boundary concentrations in the as-irradiated condition and after PIA at 550 °C for 5 and 20 h [11].

	GB Cr (wt.%)	GB Ni (wt.%)	GB Si (wt.%)
R1 (As-Irradiated)	12.8	24.0	2.48
R3 (550 °C, 5 h)	15.1	14.7	0.65
R4 (550 °C, 20 h)	16.9	13.7	0.43

anneal at this temperature. Previous work on 7.7 dpa 304 L SS also suggests that PIA treatments reduced CGR in HWC [15]. So the mitigation effect of PIA on crack propagation depends strongly on the test environment.

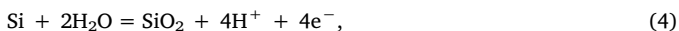
The challenge then is to identify the factors that could couple with the environment to affect IGSCC in HWC and not in NWC. It seems that mechanical behavior (yield stress or dislocation channeling) or intragranular features (loops, precipitates) are secondary factors given that they will not couple with the environment. Among the microstructure changes induced by PIA, the recovery of grain boundary segregation would be most likely to couple with the environment as well as to change with the extent of PIA to affect the intergranular SCC process. That is because the corrosion at grain boundary is affected not only by the local chemical composition, but also by the environment which determines the thermodynamic conditions (such as corrosion potential and pH). Cr depletion at grain boundaries has long been reported to decrease the SCC resistance of SS in oxygenated high temperature water [23,25]. Nevertheless, the grain boundary Cr depletion plays an insignificant role in the IGSCC of SS in hydrogenated water [25,26]. Ni enrichment is less likely to affect the SCC susceptibility as it is a less active element than Cr in corrosion. Phosphorus segregation at grain boundaries is insignificant [11] and has been reported not to influence CGR [16,24]. As such, Si segregation is the remaining composition factor that could affect the SCC propagation behavior of 304 L SS in this work.

4.2. Effect of Si on CGR in NWC vs HWC

The effect of bulk Si content on the CGR of similar materials has been studied before. Li et al. [16] reported that elevated Si content could significantly promote the CGR of austenitic steels simulating as-irradiated grain boundary compositions in PWR primary water. Andresen and Morra [17] investigated the effect of Si content on the CGR in both NWC and HWC and found that Si has little effect on the CGR of 304 L SS in NWC but could dramatically increase CGR in HWC. Although these two works focused on the bulk Si content, the effect on CGR is very consistent with that of grain boundary Si concentration in this work. Li et al. [16] proposed that Si might promote IASCC by lowering the stacking fault energy (SFE), decreasing the strength of the oxide film, or increasing the oxidation tendency. Si is an active element for oxidation, even more active than Cr. SiO₂, is normally a protective oxide on Si-bearing alloys in high temperature gaseous environment. However, recent work has shown that this oxide is subject to dissolution in high temperature water [27,28]. Consistently, Han et al. [29] reported that the oxide film formed on a model alloy containing 4.5 wt.% Si in simulated PWR primary water was porous and depleted in Si. The

decreasing strength of the oxide film in the high Si model alloy reported by Li et al. [16] may be related to a compromised oxide structure. The IGSCC growth in this work may be directly related to the oxidation and dissolution of Si at the grain boundary.

The oxidation reaction of Si in high temperature water occurs by the following reaction:



and the Nernst equation of this reaction at 288 °C is:

$$E_0 = E^0 - 0.111\text{pH} - 0.0278\log(a_{\text{Si}}), \quad (5)$$

where E_0 is the equilibrium potential, E^0 is the standard electrode potential and a_{Si} is the atomic concentration of Si. From Eq. (5), the equilibrium potential E_0 increases as Si concentration a_{Si} decreases, which means it is less likely to form SiO_2 with lower Si content. The standard electrode potential E^0 is calculated to be -1.08 V using HSC 6.0 [30]. For R4 (550 °C, 20 h) which has the lowest grain boundary Si concentration, the equilibrium potential E_0 in 288 °C neutral water ($\text{pH} \approx 5.66$) is calculated to be $-1.65 V_{\text{SHE}}$. The measured corrosion potential in either NWC or HWC (Fig. 3) is well above this value, suggesting that Si at the grain boundary would be oxidized to SiO_2 which readily dissolves. Recent work by Lou et al. [31] shows that the Si-rich oxide along the grain boundaries of additively manufactured 316 L SS preferentially dissolves in either NWC or HWC water. It is assumed here that once SiO_2 forms, it dissolves quickly into the solution. The extensive secondary intergranular cracks found on the fracture surfaces (Fig. 5) suggest that the grain boundary could crack open even when the local stress intensity was relatively low, further confirming the occurrence of fast intergranular dissolution. Hence, the controlling process of Si dissolution is the oxidation of Si by Eq. (4). The dissolution kinetics may be highly dependent on the overpotential. As Si shows no passivation in high temperature water, the anodic current would increase with increasing overpotential.

The CGR dependence on grain boundary Si concentration in HWC in this work may be linked to the change of anodic overpotential for Si oxidation. A higher Si concentration gives a lower equilibrium potential according to Eq. (5) and thus a larger overpotential if it is assumed that the H_2 generated at the crack tip would not build up significantly due to the fast refresh rate of solution in this work (~4 autoclave volumes per hour). Therefore, the anodic dissolution of Si at the crack tip and hence, the CGR in HWC, decreases with the recovery of Si segregation at grain boundary. The situation in NWC is different. The major cathodic reaction in NWC is the reduction of oxygen. The diffusion of oxygen in high temperature water is slower than hydrogen [32], especially through a confined route like an intergranular crack. The time lag in the CGR change after the HWC to NWC switch (Fig. 3) could also be related to the slow diffusion of oxygen to the crack tip. In NWC, once the oxygen at the crack tip is consumed and could not be replenished in time, the corrosion potential drops. Thus, a higher grain boundary Si concentration would consume more oxygen at the beginning and then result in a lower corrosion potential at the crack tip. Meanwhile, the equilibrium potential E_0 for Si oxidation is also lower for a higher Si concentration according to Eq. (5). Therefore, the anodic overpotential (difference between the corrosion potential and E_0) for Si oxidation at the crack tip may not change significantly. This is one reason why the CGR in NWC is insensitive to the grain boundary Si concentration.

The loss of mitigating effect of HWC on CGR of highly-irradiated SS reported in a previous work [4] may be also related to Si segregation at the grain boundary. The mitigation effect of HWC vanished at doses above ~6-7 dpa [4], at which the Si concentration at the grain boundary was measured to be ~4.5 wt.% for irradiated SS in LWR [33]. So ~4.5 wt.% may be the critical grain boundary Si concentration above which HWC has no mitigation effect on CGR. Consistently, the HWC effect was reported to vanish when the bulk Si content was 5 wt.% or above [17]. The as-irradiated sample shows a grain boundary Si concentration

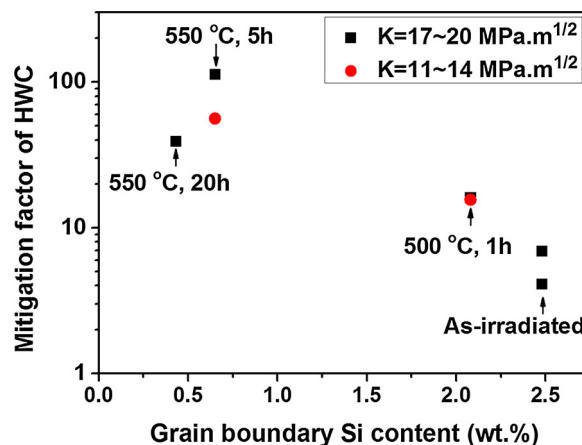


Fig. 7. Change of the mitigation factor of HWC with the grain boundary Si content.

(2.48 wt.%) below the critical level (Table 8) and HWC can still mitigate the CGR by a factor less than 10 (Table 6). The grain boundary composition for the PIA condition of R2 was not measured due to the lack of proper samples. The grain boundary Si concentration for this sample was estimated as follows. The diffusion distance of Si for each PIA condition was calculated based on the diffusion coefficient of Si in iron [34]. A curve was fit between the percentage drop in the enriched portion of grain boundary Si and the diffusion distance of Si using the available data in Table 8 on the assumption that there would be no grain boundary Si enrichment when the diffusion distance of Si is infinite. Then the acquired exponential function was used to back calculate the grain boundary Si concentration for the condition of 1 h at 500 °C which is 2.08 wt.%. Fig. 7 shows the change of mitigation factor with the grain boundary Si content. As the grain boundary Si concentration decreases with the severity of PIA treatment, the mitigation factor of HWC increases continuously up to 5 h at 550 °C.

The combination of HWC and PIA is necessary to mitigate the CGR of neutron-irradiated SS in BWR. It is reasonable to predict that PIA can also suppress the CGR in a simulated PWR primary environment which is a reducing environment like HWC. In fact, the tests by Li et al. [16] were conducted in a simulated PWR primary water environment and a similar effect of bulk Si concentration on CGR was revealed.

4.3. Comparison of IASCC susceptibility in CGR and CERT tests

The CERT test results clearly show that PIA significantly suppresses the SCC susceptibility of this batch of samples in NWC (Fig. 8) [35] except the 20 h at 550 °C condition, which resulted in sensitization at some grain boundaries [13]. The striking difference in sensitivity of CERT and CGR results to PIA condition implies that different factors are controlling the SCC initiation and propagation processes. In CERT test, the controlling process is crack initiation in round tensile bars which have no confined diffusion path as in compact tension sample. So the mixed potential of CERT sample is directly related to the dissolved oxygen concentration and would be uniform across the sample surface. Thus, the local anodic overpotential for Si oxidation at the exposed grain boundary decreases as the local Si concentration decreases with higher severity of PIA condition. As a result, the Si dissolution rate and the SCC susceptibility drop after PIA. It should be noted that all CERT specimens in which a crack initiated, regardless of the PIA condition, displayed a large amount of IG area on the fracture surface [13], indicating that the cracks grew at a relative rapid rate once initiated, consistent with the CGR results shown here. Given that PIA has different effects on crack initiation and propagation, it is suggested that CGR test is indispensable in assessing the full effect of PIA on the SCC initiation and propagation of neutron-irradiated material.

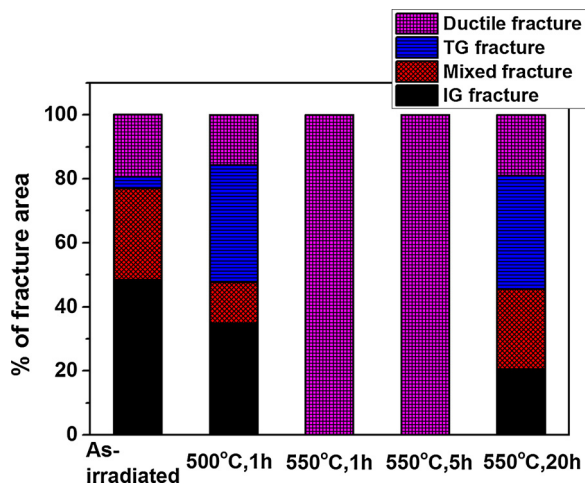


Fig. 8. Change in the fracture morphology of 304L SS irradiated to 5.9 dpa after CERT test in NWC water [35].

5. Conclusions

This work studied the effects of PIA on CGR of neutron-irradiated SS in simulated BWR environments. In contrast to the results from CERT tests, the CGR results show that PIA has little effect on the crack propagation susceptibility in NWC environment, even after most of the irradiation-induced microstructure change was restored. Nevertheless, it can significantly suppress the CGR in HWC. The mitigation factor of HWC increases from less than 10 to near two orders of magnitude with the severity of PIA treatments up to 5 h at 550 °C. The decrease in SCC propagation susceptibility in HWC is closely related to the recovery of Si segregation at grain boundary, as Si can oxidize and dissolve into solution, creating a defective oxide structure. PIA can effectively mitigate the IASCC propagation in combination with HWC in BWR and likely in PWR primary environment.

Data availability

The raw/processed data required to reproduce these findings cannot be shared at this time as the data also forms part of an ongoing study.

Acknowledgements

The authors gratefully acknowledge financial support through the DOE NEUP, contract DE-AC07-05ID14517 and the DOE LWRs program, contract DE-AC05-00OR22725. The authors would like to thank Alex Flick and Philip Simpson from the University of Michigan for their technical assistance in the crack growth rate test in the Irradiated Materials Testing Laboratory. The authors are grateful to Peter Andresen for his help in conducting the test and discussion on the results.

References

- G.S. Was, P.L. Andresen, Stress corrosion cracking behavior of alloys in aggressive nuclear reactor core environments, *Corrosion* 63 (2007) 19–45.
- F.P. Ford, B.M. Gordon, R.M. Horn, *ASM Handbook. Corrosion in Boiling Water Reactor vol. 13C*, ASM International, 2006.
- P.L. Andresen, M.M. Morra, IGSCC of non-sensitized stainless steels in high temperature water, *J. Nucl. Mater.* 383 (2008) 97–111.
- J. Anders, BWR Vessels and Internals Project, Crack Growth in High Fluence BWR Materials-phase 1: Crack Growth Rate Testing of Types 304L and 316L at Doses Ranging From 3.5 to 13 Dpa, EPRI, Palo Alto, CA, 2009 1019079.
- O.K. Chopra, A.S. Rao, A review of irradiation effects on LWR core internal materials – IASCC susceptibility and crack growth rates of austenitic stainless steels, *J. Nucl. Mater.* 409 (2011) 235–256.
- R. Katsura, Y. Ishiyama, N. Yokota, T. Kato, K. Nakata, K. Fukuya, H. Sakamoto, K. Asano, Post-irradiation annealing effect of austenitic stainless steels in IASCC, *CORROSION* 98

- NACE International, San Diego, California, 1998.
- K. Fukuya, M. Nakano, K. Fujii, T. Torimaru, Y. Kitsunai, Separation of Microstructural and microchemical effects in irradiation assisted stress corrosion cracking using post-irradiation annealing, *J. Nucl. Sci. Technol.* 41 (2004) 1218–1227.
- A. Jacobs, S. Dumbill, Effects of low-temperature annealing on the microstructure and grain boundary chemistry of irradiated type 304SS and correlation with IASCC, 7th International Conference on Environmental Degradation of Materials in Nuclear Power Systems (1995) 1021–1031.
- W. Van Renterghem, A. Al Mazouzi, S. Van Dyck, Influence of post irradiation annealing on the mechanical properties and defect structure of AISI 304 steel, *J. Nucl. Mater.* 413 (2011) 95–102.
- W. Van Renterghem, M.J. Konstantinović, M. Vankeerberghen, Evolution of the radiation-induced defect structure in 316 type stainless steel after post-irradiation annealing, *J. Nucl. Mater.* 452 (2014) 158–165.
- Z. Jiao, J. Hesterberg, G.S. Was, Effect of post-irradiation annealing on the irradiated microstructure of neutron-irradiated 304L stainless steel, *J. Nucl. Mater.* 500 (2018) 220–234.
- A.J. Jacobs, G.P. Wozadlo, G.M. Gordon, Low-temperature annealing: a process to mitigate irradiation-assisted stress corrosion cracking, *Corrosion* 51 (1995) 731–737.
- J. Hesterberg, Z. Jiao, G.S. Was, Effects of post-irradiation annealing on the IASCC susceptibility of neutron-irradiated 304L stainless steel, *J. Nucl. Mater.* 526 (2019) 151755.
- R. Pathania, R. Carter, R. Horn, P.L. Andresen, Crack growth rates in irradiated stainless steels in BWR internals, 14th Int. Conf. on Environmental Degradation of Materials in Nuclear Power Systems, Virginia Beach, VA, 2009.
- Y. Chimi, Final Report on the BWR Crack Growth Rate Investigation IFA-745, (2014).
- G.F. Li, Y. Kaneshima, T. Shoji, Effects of impurities on environmentally assisted crack growth of solution-annealed austenitic steels in primary water at 325°C, *Corrosion* 56 (2000) 460–469.
- P.L. Andresen, M.M. Morra, Effects of Si on SCC of irradiated and unirradiated stainless steels and nickel alloys, Proceedings of the 12th International Conference on Environmental Degradation of Materials in Nuclear Power System, Salt Lake City, UT, USA, 2005.
- M.B. Toloczko, P.L. Andresen, S.M. Bruemmer, SCC crack growth of cold-worked type 316 SS in simulated BWR oxidizing and hydrogen water chemistry conditions, 13th International Conference on Environmental Degradation of Materials in Nuclear Power Systems, Whistler, British Columbia, 2007.
- P.L. Andresen, M.M. Morra, K. Ahluwalia, SCC of alloy 152/52/52i weld metals in PWR primary water, Proceedings of the 16th International Conference on Environmental Degradation of Materials in Nuclear Power Systems-Water Reactors, Asheville, North Carolina, USA, 2013.
- A. Jessen, P. Chou, C. Tobpasi, Effect of specimen size on the crack growth rate behavior of irradiated type 304 stainless steel, Proceedings of the 18th International Conference on Environmental Degradation of Materials in Nuclear Power Systems – Water Reactors, Portland, OR, USA, 2017.
- K. Arioka, T. Yamada, T. Terachi, G. Chiba, Cold work and temperature dependence of stress corrosion crack growth of austenitic stainless steels in hydrogenated and oxygenated high-temperature water, *Corrosion* 63 (2007) 1114–1123.
- M.D. McMurtrey, B. Cui, I. Robertson, D. Farkas, G.S. Was, Mechanism of dislocation channel-induced irradiation assisted stress corrosion crack initiation in austenitic stainless steel, *Curr. Opin. Solid State Mater. Sci.* 19 (2015) 305–314.
- S.M. Bruemmer, Grain boundary composition effects on environmentally induced cracking of engineering materials, *Corrosion* 44 (1988) 364–370.
- P.L. Andresen, C.L. Briant, Role of S, P and N segregation on intergranular environmental cracking of stainless steels in high temperature water, Proceedings of the Third International Symposium on Environmental Degradation of Materials in Nuclear Power Systems-Water Reactors, The Metallurgical Society, Traverse City, Michigan, 1987.
- S.M. Bruemmer, G.S. Was, Microstructural and microchemical mechanisms controlling intergranular stress corrosion cracking in light-water-reactor systems, *J. Nucl. Mater.* 216 (1994) 348–363.
- K. Arioka, T. Yamada, T. Terachi, R.W. Staehle, Intergranular stress corrosion cracking behavior of austenitic stainless steels in hydrogenated high-temperature water, *Corrosion* 62 (2006) 74–83.
- P.J. Doyle, S.S. Raiman, R. Rebak, K.A. Terrani, Characterization of the hydrothermal corrosion behavior of ceramics for accident tolerant fuel cladding, 18th International Conference on Environmental Degradation of Materials in Nuclear Power Systems-Water Reactors, Portland, OR, USA, 2017.
- K.A. Terrani, Y. Yang, Y.J. Kim, R. Rebak, H.M. Meyer, T.J. Gerczak, Hydrothermal corrosion of SiC in LWR coolant environments in the absence of irradiation, *J. Nucl. Mater.* 465 (2015) 488–498.
- G. Han, Z. Lu, X. Ru, J. Chen, J. Zhang, T. Shoji, Properties of oxide films formed on 316L SS and model alloys with modified Ni, Cr and Si contents in high temperature water, *Corros. Sci.* 106 (2016) 157–171.
- HSC 6.0, Outokumpu Research Oy Information Service.
- X. Lou, P.L. Andresen, R.B. Rebak, Oxide inclusions in laser additive manufactured stainless steel and their effects on impact toughness and stress corrosion cracking behavior, *J. Nucl. Mater.* 499 (2018) 182–190.
- D.T. Kallikragas, A.Y. Plugatyr, I.M. Svishchev, High temperature diffusion coefficients for O₂, H₂, and OH in water, and for pure water, *J. Chem. Eng. Data* 59 (2014) 1964–1969.
- D. Edwards, E. Simonen, S. Bruemmer, Radiation-induced segregation behavior in austenitic stainless steels: fast reactor versus light water reactor irradiations, 13th International Conference on Environmental Degradation of Materials in Nuclear Power Systems, Whistler, British Columbia, 2007.
- H.V.M. Mirani, P. Maaskant, Diffusion of Si in Fe-Si containing 8 to 11 at% Si, *Phys. Status Solidi (A)* 14 (1972) 521–525.
- G.S. Was, W. Kuang, R. Bhambroo, J. Hesterberg, Program on Technology Innovation: Toward Predictive Modeling and Mitigation of Irradiation Assisted Stress Corrosion Cracking of Austenitic Steels in LWR Core Components, (2018).